Self-Tuning Dual-Layer Sliding Mode Control of Electromagnetic Suspension System

Hong-Wei Li, Duo Zhang, Yang Lu, Yi-Qing Ni, *Member, IEEE*, Zhao-Dong Xu, Qi Zhu, and Su-Mei Wang, *Member, IEEE*

***Abstract*— The suspension system in electromagnetic suspension maglev trains is highly nonlinear and sensitive to uncertainties, noise, and disturbances, making it quite challenging to design the proper electromagnetic voltages to control the suspension gap. In this paper, a self-tuning dual-layer sliding mode control system (SD-SMC) is developed to control the electromagnetic suspension system where voltage saturation, sensor noise, and a wide range of parametric uncertainties/variations exist. SD-SMC consists of dual-layer sliding mode controllers, a delay-compensated low-pass filter, and a forgetting least-squares estimator. Compared with existing control systems, SD-SMC can achieve high performance under large model uncertainties and disturbances with relatively low control voltages, and meanwhile, the control chattering and overshooting issues can be well mitigated. Both numerical and experimental examples are investigated to validate the proposed control system.**

***Index Terms*— Maglev suspension system, sliding mode control, adaptive control, robust control, model uncertainties, online estimator.**

I. Introduction

MAGLEV trains have attracted increasing attention due to their advantages of safety, comfort, low noise, etc [1], [2], [3], [4], [5], [6]. Unlike traditional rail systems, maglev trains operate without physical contact between the train and the track, utilizing powerful magnetic fields to achieve levitation and propulsion. This innovative approach significantly reduces friction, allowing for unprecedented speeds and smoother rides. The integration of maglev technology into the broader intelligent transportation system has the potential to revolutionize urban and intercity travel by enhancing connectivity, reducing travel times, and minimizing environmental impact. Maglev trains are poised to play a pivotal role in shaping the future of transportation infrastructure.

There are mainly two types of maglev trains: the electrodynamic suspension (EDS) train and the electromagnetic suspension (EMS) train [1], [7]. For the EDS train, the train is suspended by repulsive forces generated from permanent or superconducting magnets; and for the EMS train, the train is suspended by attractive forces generated from electromagnets. Because the suspension force is proportional to the current square and inversely proportional to the air gap square in an EMS system, and there are also complicated relationships among the current, air gap, and voltage, the design of the command voltage to achieve a designated air gap for the EMS system is essentially a highly nonlinear control problem that demands carefully designed controllers or control systems.

Many control methods have been implemented for EMS control problems. Based on linearized models of EMS systems, the proportional-integral-derivative (PID) controller [8], [9], the linear quadratic regulator (LQR) controller [10], the H_∞ controller [11], and the deep learning based semi-supervised controller [12], etc., have been successfully deployed. However, these controllers can only work properly in limited ranges around the equilibrium point. Although some decentralized controllers [13], [14] or the nonlinearity compensator for the linear controller [15] can release this restriction to some extent, there is still room for improvement regarding the control performance. Fuzzy logic controllers have also been used to maintain the iron ball position in an EMS system, where good stabilization performance is observed [16], [17].

To deal with model uncertainties in EMS control problems, model-based nonlinear control techniques are required. Robust control and adaptive control are two main types of control methods that can handle model uncertainties [18], [19]. In robust control, nominal model parameters and the boundaries of these parameters are assumed to be known. Therefore, considering parametric uncertainties, the control command is formed with the normal command deduced from the nominal model and the correction command considering parametric uncertainties. In adaptive control, an adaption law is required to update the model parameters either based on the input and output signals of the control plant (self-turning adaptive control), or the output deviations between the ideal model constructed for reference and the control plant

Received 25 March 2024; revised 22 July 2024 and 17 November 2024; accepted 28 November 2024. Date of publication 16 December 2024; date of current version 4 February 2025. This work was supported in part by the Start-Up Fund for Research Assistant Professors under the Strategic Hiring Scheme of The Hong Kong Polytechnic University under Grant P0046770; in part by Wuyi University's Hong Kong and Macao Joint Research and Development Fund under Grant 2021WGALH15; and in part by the Innovation and Technology Commission of Hong Kong SAR Government to Hong Kong Branch of the National Engineering Research Center on Rail Transit Electrification and Automation under Grant K-BBY1. The Associate Editor for this article was A. Nunez. *(Corresponding author: Yi-Qing Ni.)*

Hong-Wei Li, Duo Zhang, Yang Lu, Yi-Qing Ni, Qi Zhu, and Su-Mei Wang are with the Department of Civil and Environmental Engineering, National Rail Transit Electrification and Automation Engineering Technology Research Center (Hong Kong Branch), The Hong Kong Polytechnic University, Hong Kong, China (e-mail: hong-wei.li@polyu.edu.hk; duo-dz.zhang@polyu.edu.hk; luyang.y.lu@polyu.edu.hk; ceyqni@polyu.edu.hk; qi-sue1.zhu@connect.polyu.hk; may.sm.wang@polyu.edu.hk).

Zhao-Dong Xu is with the School of Civil Engineering, China–Pakistan Belt and Road Joint Laboratory on Smart Disaster Prevention of Major Infrastructures, Southeast University, Nanjing 210096, China (e-mail: zhdxu@163.com).

Digital Object Identifier 10.1109/TITS.2024.3509997

(model-reference adaptive control). The sliding mode controller is one of the most representative of robust controllers and has been widely applied to EMS problems, see [20], [21], [22], [23], while the control chattering (oscillations of the system dynamics across the sliding surface), which is one of the most significant issues of sliding mode controllers, remains in these studies. Some researchers combined sliding mode controllers with adaptive control methods aiming to avoid overcontrol by tuning the switch gain in the correction command [24], [25], [26]. The limitation is that these methods cannot compensate for model uncertainties well and thus might still lead to large and rapid changes in the switch gain when large uncertainties exist. An adaptive radial-basis-function-neural-network compensator was combined with the sliding mode controller for a reluctance-motor maglev system [27], where the entire control system can not only compensate for uncertainties but also reduce overestimation. Nevertheless, sensor noise was not considered in this work, and the maglev system took the current rather than the voltage as the command signal, which simplified the control problem. The adaptive terminal sliding mode controller (AT-SMC), adaptive backstepping sliding mode controller, and adaptive integral backstepping sliding mode controller were developed to design the electromagnetic voltage to realize the iron ball suspension [28], where the AT-SMC performed the best among them in terms of reducing the convergence time and rejecting the control chattering. The super-wisting SMC derived from the high-order sliding mode control theory has also been established for the same ball suspension system, which achieved good performance in the presence of disturbances [29]. However, these controllers require full states (ball position, ball momentum, and electromagnetic inductance) of the system. The abovementioned studies indicate how to design a suspension controller/control system for maglev trains that could perform well regardless of large model uncertainties, limited measurements with noise, external disturbances, etc., still deserves in-depth investigations, which is exactly the motivation and objective of the present work.

In this paper, robust and adaptive control techniques are incorporated in a novel way to realize the abovementioned control objective for EMS medium- or low-speed maglev trains. A self-tuning dual-layer sliding mode control system (SD-SMC) including dual-layer sliding mode controllers, a delay-compensated low-pass (DCLP) filter, and a forgetting least-squares (FL) estimator is developed, considering influences of model uncertainties, sensor noise, voltage saturation, and train force variations. To accomplish the voltage design for the suspension gap stabilization, the first layer controller calculates the required current signal, which is then treated as the control target of the second layer controller to generate the command voltage. The dual-layer sliding mode controllers are robust to model uncertainties/variations, and the FL estimator can further improve the control precision and reduce the chattering level by updating the control plant. Additionally, the DCLP filter is adopted to deal with sensor noise. Both numerical examples and experimental examples are carried out, demonstrating that high performance of the control system can be achieved.

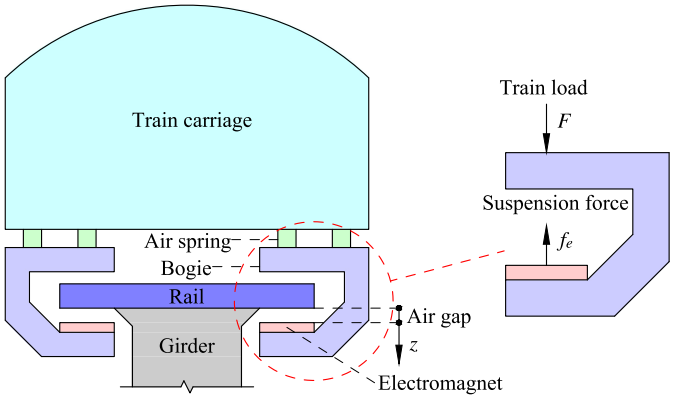

Fig. 1. Schematic diagram of the EMS maglev train.

II. Problem Description

Fig. 1 shows the schematic diagram of the EMS maglev train. A maglev train carriage is supported by several pairs of bogies. When the train is running along the rail track, the electromagnet attached to the bogie generates an attractive force acting on the iron rail track above the electromagnet, and in turn, a suspension force is applied to the electromagnet to lift the bogie and the train carriage. The suspension bogie is the system that will be investigated in this paper.

The suspension force f_e can be expressed as

$$f_e(I,z)=\frac{\mu_0 A_e N_e^2}{4}\cdot\frac{I^2}{z^2}=C\frac{I^2}{z^2} \tag{1}$$

where I is the current in the electromagnetic coil; z is the air gap between the electromagnet and the rail track, i.e., the displacement of the electromagnet relative to the rail track ($z>0$); $\mu_0=4\pi\times10^{-7}\mathrm{N\cdot A^{-2}}$ is the permeability of vacuum; A_e is the effective polar area of the electromagnetic coil; and N_e is the number of the electromagnetic coil turns. The bogie's equation of motion is

$$m\ddot{z}+f_e=F \tag{2}$$

where m is the mass of the bogie; F is the train load including the uncertain force from the carriage and bogie. The electromagnetic voltage u is given by

$$u=RI+2C\frac{\mathrm{d}(I/z)}{\mathrm{d}t}=RI+\frac{2C}{z}\dot{I}-\frac{2CI}{z^2}\dot{z} \tag{3}$$

There are uncertainties on parameters C and R, and variations on the parameter F. The measurements are assumed to be the gap (displacement) z_m, acceleration $\ddot{z}_m$, and current I_m. Sensor noise exists in z_m and $\ddot{z}_m$. The control target is to design the voltage signal u for the highly nonlinear EMS system to stabilize the air gap around a pre-designated value z_d, regardless of uncertainties/variations, voltage saturation, and sensor noise. Additionally, the equilibrium of the EMS system itself is unstable, necessitating very strict requirements for the control system.

The major limitation of the suspension model examined in this paper is that it only accounts for the vertical translational movement of the bogie levitation point while can not consider other types of movements, such as rolling (rotation along

the x-axis), and pitching (rotation along the y-axis) of the entire train bogie and the train carriage above it. In addition, except for the suspension system illustrated in Fig. 1, an EMS maglev train also has guidance and propulsion systems that may affect the suspension system. However, these influences are not significant and can be regarded as minor disturbances in modeling the suspension system because these systems operate independently in perpendicular directions. There are previous studies that established a 2-DOF model for the bogie considering two suspension points [13], [30], [31] or formed a 3-DOF model using four suspension points [8]. Since all suspension points exert vertical attractive forces, the bogie can be segmented into several parts around the suspension points. For each suspension point, an individual 1DOF model can be established. The static train load from the train carriage and bogie acting on the levitation point and the model mass can be calculated according to the number of suspension points. The primary assumption or precondition for this simplification is that the main movements of the bogie relative to the rail are vertical translational movements within a certain range. This condition is met due to the construction of the maglev train system, where the bogie is securely locked onto the rail track. This simplified modeling approach is acceptable for investigating suspension control systems of EMS trains and has been adopted in many previous studies [12], [14], [32], [33], [34]. Therefore, the 1DOF model as shown in equations 1-3 is adopted in this paper, where F is the uncertain force containing all the forces and disturbances from the bogie and train.

III. Control System Design

The control system SD-SMC includes dual-layer sliding mode controllers, a DCLP filter, and an FL estimator, which will be presented in detail below.

A. Dual-Layer Sliding Mode Controllers

Two sliding mode controllers are implemented respectively. The idea is to design the current command I_d to realize the air gap stabilization (first layer), then take I_d as the designated current trajectory to design the control voltage u (second layer).

1) First Layer Controller: Combining equations 1 and 2 yields

$$\ddot{z} = a - bh \tag{4}$$

where

$$a = \frac{F}{m} > 0,\ \ b = \frac{C}{m} > 0,\ \ h = \frac{I^2}{z^2} \geq 0. \tag{5}$$

Equation 4 is treated as the control plant in this layer. The parameters a and b contain uncertainties, and their nominal values are assumed to be $\hat{a}$ and $\hat{b}$ ($\hat{a} > 0,\ \hat{b} > 0$). Additionally, the differences between their nominal and true values are assumed to be bounded, i.e.,

$$|a - \hat{a}| \leq \bar{a},\ \ |b - \hat{b}| \leq \bar{b}, \tag{6}$$

where $\bar{a}$ and $\bar{b}$ are corresponding parameter error boundaries.

Define the compact error E_z as

$$E_z = \dot{e}_z + \lambda_z e_z = \dot{z} - \dot{z}_d + \lambda_z (z - z_d) \tag{7}$$

where $e_z = z - z_d$ is the displacement tracking error, and λ_z is a control bandwidth (positive value). A large λ_z is preferred because it would cause more control efforts to minimize the compact error. Meanwhile, a large λ_z can also produce high-frequency dynamics in the system, amplifying the negative effects of disturbances and sensor noise. λ_z typically should not exceed three values as below [18]

$$\lambda_z \leq \frac{2\pi}{3}\omega_R,\ \ \lambda_z \leq \frac{1}{3T_A},\ \ \lambda_z \leq \frac{f_s}{5}, \tag{8}$$

where ω_R is the frequency of the lowest unmodeled resonant mode, T_A is the largest unmodeled time-delay, and f_s is the sampling rate. In this paper, λ_z is initially set to $f_s/5$ and is gradually reduced (if needed) through trial and error. It can be proven that the boundedness of E_z is equivalent to the boundedness of e_z [18], therefore, the control target is equivalent to driving the compact error E_z to the sliding surface $E_z = 0$. A straightforward strategy to achieve that is to make

$$\left.\begin{aligned} \dot{E}_z &\leq -\eta_z \text{ for } E_z \geq 0 \\ \dot{E}_z &\geq \eta_z \text{ for } E_z < 0 \end{aligned}\right\} \ \text{i.e.,}\ \ \dot{E}_z E_z \leq -\eta_z |E_z| \tag{9}$$

where η_z is a positive constant. Equation 9 is defined as the *sliding rule*, and it can also be explained by the Lyapunov stability theory [18]. The energy-type Lyapunov function (positive definite and radially unbounded) can be taken as $V_z = E_z^2/2$. To guarantee the system's stability given a control command h, the time derivative of V_z, i.e., $\dot{V}_z = \dot{E}_z E_z$, must be negative, which leads to equation 9.

The command signal h is formed as

$$h = \hat{h} + h_c \tag{10}$$

where $\hat{h}$ is the nominal command to achieve $\dot{E}_z = 0$ assuming that no parametric uncertainties exist in the control plant, i.e., the parameters of the control plant are $\hat{a}$ and $\hat{b}$; h_c is the command correction to avoid potential perturbations caused by the model uncertainties. Since

$$\begin{aligned} \dot{E}_z &= \dddot{z} - \dddot{z}_d + \lambda_z(\ddot{z} - \ddot{z}_d) = a - bh + \rho, \\ \rho &= -\dddot{z}_d + \lambda_z(\ddot{z} - \ddot{z}_d), \end{aligned} \tag{11}$$

it can be obtained from $\hat{a} - \hat{b}\hat{h} + \rho = 0$ that

$$\hat{h} = \hat{b}^{-1}(\hat{a} + \rho). \tag{12}$$

The command correction is designed as

$$h_c = k_z \text{sgn}(E_z) = \begin{cases} k_z \text{ for } E_z \geq 0 \\ -k_z \text{ for } Ez < 0 \end{cases} \tag{13}$$

Therefore

$$\begin{aligned} \dot{E}_z &= a - b\left[\hat{b}^{-1}(\hat{a} + \rho) + k_z \text{sgn}(E_z)\right] + \rho \\ &= -bk_z \text{sgn}(E_z) + a - \hat{a} + (\hat{b} - b)\hat{h}. \end{aligned} \tag{14}$$

$\dot{E}_z E_z \leq -\eta_z |E_z|$ and $\text{sgn}(E_z)E_z = |E_z|$ result in

$$k_z |E_z| \geq b^{-1}(a - \hat{a})E_z + b^{-1}(\hat{b} - b)\hat{h}E_z + b^{-1}\eta_z |E_z|. \tag{15}$$

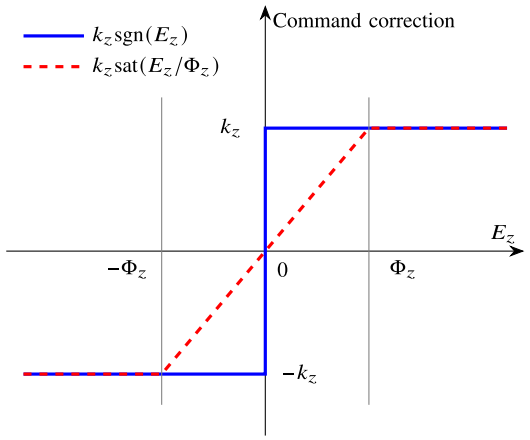

Fig. 2. Command correction with (dashed line) and without (solid line) using the boundary layer for $k_z > 0$.

Because

$$\frac{\bar{a}}{\hat{b}-\bar{b}}|E_z| \geq b^{-1}(a-\hat{a})E_z,\ \ \frac{\eta_z}{\hat{b}-\bar{b}}|E_z| \geq b^{-1}\eta_z|E_z|,$$
$$\frac{\bar{b}}{\hat{b}-\bar{b}}|\hat{h}|\cdot|E_z| \geq b^{-1}(\hat{b}-b)\hat{h}E_z, \tag{16}$$

the value of k_z that satisfies equation 15 can be set to

$$k_z = \frac{1}{\hat{b}-\bar{b}}\left(\bar{a}+\bar{b}|\hat{h}|+\eta_z\right). \tag{17}$$

Equations 10, 12, 13 and 17 determine the control command. However, the term $\text{sgn}(E_z)$ tends to cause a relatively high level of chattering, which could excite the high-frequency dynamics ignored in the model of the control plant or even might drive the system unstable [35]. To make the control command more smooth, a boundary layer Φ_z ($\Phi_z > 0$) is created around the sliding surface, and the command correction is modified as

$$h_c = k_z\text{sat}\left(\frac{E_z}{\Phi_z}\right) = \begin{cases} k_z E_z/\Phi_z \text{ for } |E_z| < \Phi_z \\ k_z\text{sgn}(E_z) \text{ for } |E_z| \geq \Phi_z \end{cases} \tag{18}$$

Fig. 2 illustrates how the boundary layer smoothes the command correction. Two cases: (a). $|E_z| < \Phi_z$, i.e., the compact error is inside the boundary layer; and (b). $|E_z| \geq \Phi_z$, i.e., the compact error is outside the boundary layer, are discussed below.

(a). $|E_z| < \Phi_z$.

Equation 14 becomes

$$\dot{E}_z + \frac{bk_z}{\Phi_z}E_z = a - \hat{a} + (\hat{b}-b)\hat{h}, \tag{19}$$

which can be regarded as a first-order low-pass filter on the compact error E_z, where the input $a-\hat{a}+(\hat{b}-b)\hat{h}$ is the perturbation caused by model uncertainties. The filter's cut-off frequency bk_z/Φ_z satisfies

$$\frac{bk_z}{\Phi_z} \leq \frac{(\hat{b}+\bar{b})k_z}{\Phi_z} = f_z \tag{20}$$

where f_z is the preset frequency limit. A higher cut-off frequency is preferred because it leads to a lower filter gain, which can more effectively stabilize the compact error. However, the cut-off frequency cannot be too high, as this would compromise the filter's "low-pass" characteristics and could introduce unmodeled high-frequency dynamics into the system. Therefore, f_z should be selected within a reasonable range. Based on the simulation results, a possible choice is to set $f_z = 0.5\lambda_z \sim \lambda_z$. Equation 20 gives the relationship between k_z and Φ_z as follows

$$k_z = \frac{f_z}{\hat{b}+\bar{b}}\Phi_z. \tag{21}$$

(b). $|E_z| \geq \Phi_z$.

The width of the boundary layer is designed to be changeable ($\dot{\Phi}_z \neq 0$), and the sliding rule is modified as

$$\left.\begin{aligned} \dot{E}_z - \dot{\Phi}_z \leq -\eta_z \text{ for } E_z \geq \Phi_z \\ \dot{E}_z + \dot{\Phi}_z \geq \eta_z \text{ for } E_z \leq -\Phi_z \end{aligned}\right\} \text{i.e., } \dot{E}_z E_z \leq (\dot{\Phi}_z - \eta_z)|E_z| \tag{22}$$

which can be interpreted that the distance between the compact error and the boundary layer always tends to decrease when the compact error is outside the boundary layer. Equation 22 also reflects the pattern that the compact error stabilization process is less stringent during boundary layer expansion ($\dot{\Phi}_z > 0$), and more stringent during boundary layer contraction ($\dot{\Phi}_z < 0$). Following the similar derivation procedure from equations 14 to 17, the value of k_z that satisfies equation 22 could be selected as

$$k_z = \frac{\bar{a}+\bar{b}|\hat{h}|}{\hat{b}-\bar{b}} + \begin{cases} \frac{1}{\hat{b}-\bar{b}}\left(\eta_z - \dot{\Phi}_z\right) \text{ for } \eta_z \geq \dot{\Phi}_z \\ \frac{1}{\hat{b}+\bar{b}}\left(\eta_z - \dot{\Phi}_z\right) \text{ for } \eta_z < \dot{\Phi}_z \end{cases} \tag{23}$$

Combining equations 21 and 23 results in the adaption formulas for the online tuning of k_z and Φ_z with their initial values being set to $k_z(0) = 0$ and $\Phi_z(0) = 0$. The adaption formulas are essentially first-order exponentially stable filters, thus the boundedness of k_z and Φ_z can be guaranteed. The compact error E_z will be stabilized whether inside or outside the boundary layer. Equations 10, 12, 18, 21 and 23 determine the modified control command with the adoption of the boundary layer. The controller generates high correction commands when the compact error is outside the boundary layer and works gently when the compact error is inside the boundary layer. Therefore, the unwanted chattering could be mitigated greatly.

Since a negative value of h is not allowed ($h = I^2/z^z > 0$), the designated current signal I_d that will be used in the second layer controller is formed as

$$I_d = \begin{cases} z\sqrt{h} \text{ for } h > 0 \\ 0 \text{ for } h \leq 0 \end{cases} \tag{24}$$

2) Second Layer Controller: Equation 3 leads to

$$\dot{I} = \left(\frac{\dot{z}}{z} - \frac{Rz}{2C}\right)I + \frac{z}{2C}u, \tag{25}$$

which is the control plant in this layer. The parameters R and C contain uncertainties, and their nominal values are assumed

to be $\hat{R}$ and $\hat{C}$ ($\hat{R} > 0$, $\hat{C} > 0$). The differences between their nominal and true values are assumed to be bounded, i.e.,

$$|R - \hat{R}| \le \bar{R}, \ |C - \hat{C}| \le \bar{C}, \tag{26}$$

where $\bar{R}$ and $\bar{C}$ are corresponding parameter error boundaries ($\hat{C} = m\hat{b}$, $\bar{C} = m\bar{b}$). The tracking error of the current is $e_i = I - I_d$, therefore

$$\dot{e}_i = \left(\frac{\dot{z}}{z} - \frac{Rz}{2C}\right) I + \frac{z}{2C}u - \dot{I}_d = \frac{z}{2C}\left(u - RI - C\sigma\right), \tag{27}$$

where

$$\sigma = -\frac{2\dot{z}}{z^2} I + \frac{2}{z}\dot{I}_d. \tag{28}$$

The command signal u is formed as

$$u = \hat{u} - u_c \tag{29}$$

where $\hat{u}$ is the nominal command to achieve $\dot{e}_i = 0$ assuming that no parametric uncertainties exist in the control plant, i.e., the parameters of the control plant are $\hat{R}$ and $\hat{C}$; u_c is the command correction to reject potential perturbations caused by the model uncertainties. It can be deduced from equation 27 that

$$\hat{u} = \hat{R}I + \hat{C}\sigma. \tag{30}$$

The command correction is designed as

$$u_c = k_i \mathrm{sat}\left(\frac{e_i}{\Phi_i}\right) = \begin{cases} k_i e_i/\Phi_i \ \text{for} \ |e_i| < \Phi_i \\ k_i \mathrm{sgn}(e_i) \ \text{for} \ |e_i| \ge \Phi_i \end{cases} \tag{31}$$

where k_i is the correction gain and Φ_i is the boundary layer ($\Phi_i > 0$). Still, two cases: (a). $|e_i| < \Phi_i$, i.e., the error is inside the boundary layer; and (b). $|e_i| \ge \Phi_i$, i.e., the error is inside the boundary layer, are discussed below.

(a). $|e_i| < \Phi_i$.

Equations 27-31 yields

$$\dot{e}_i + \frac{k_i z}{2C\Phi_i} e_i = \frac{zI}{2C}(\hat{R} - R) + \frac{z\sigma}{2C}(\hat{C} - C), \tag{32}$$

which acts as a first-order low-pass filter on e_i. The filter's cut-off frequency $k_i z/(2C\Phi_i)$ satisfies

$$\frac{k_i z}{2C\Phi_i} \le \frac{k_i z}{2(\hat{C} - \bar{C})\Phi_i} = f_i \tag{33}$$

where f_i is the preset frequency limit. Similar to f_z, the selection of f_i also involves a trade-off. However, simulation results indicate that the control system is less sensitive to f_i. One option is to set $f_i = 0.5 f_z \sim f_z$. The relationship between k_i and Φ_i is given by

$$k_i = \frac{2(\hat{C} - \bar{C}) f_i}{z}\Phi_i. \tag{34}$$

(b). $|e_i| \ge \Phi_i$.

The sliding rule is designed as

$$\dot{e}_i e_i \le (\dot{\Phi}_i - \eta_i)|e_i| \tag{35}$$

where η_i is a positive constant. Therefore

$$\dot{e}_i = \frac{zI}{2C}(\hat{R} - R) + \frac{z\sigma}{2C}(\hat{C} - C) - \frac{k_i z}{2C}\mathrm{sgn}(e_i). \tag{36}$$

Putting equation 36 into equation 35 results in

$$k_i|e_i| \ge I(\hat{R} - R)e_i + \sigma(\hat{C} - C)e_i + \frac{2C(\eta_i - \dot{\Phi}_i)}{z}|e_i|. \tag{37}$$

Because $I\bar{R}|e_i| \ge I(\hat{R} - R)e_i$, $|\sigma|\bar{C}|e_i| \ge \sigma(\hat{C} - C)e_i$, and

$$\begin{aligned} &\frac{2(\hat{C} + \bar{C})(\eta_i - \dot{\Phi}_i)}{z}|e_i| \ge \frac{2C(\eta_i - \dot{\Phi}_i)}{z}|e_i| \ \text{for} \ \eta_i \ge \dot{\phi}_i \\ &\frac{2(\hat{C} - \bar{C})(\eta_i - \dot{\Phi}_i)}{z}|e_i| \ge \frac{2C(\eta_i - \dot{\Phi}_i)}{z}|e_i| \ \text{for} \ \eta_i < \dot{\phi}_i, \end{aligned} \tag{38}$$

the selection of k_i that satisfies equation 37 could be

$$k_i = I\bar{R} + |\sigma|\bar{C} + \begin{cases} \dfrac{2(\hat{C} + \bar{C})(\eta_i - \dot{\Phi}_i)}{z} \ \text{for} \ \eta_i \ge \dot{\phi}_i \\ \dfrac{2(\hat{C} - \bar{C})(\eta_i - \dot{\Phi}_i)}{z} \ \text{for} \ \eta_i < \dot{\phi}_i \end{cases} \tag{39}$$

Combining equations 34 and 39 results in the adaption formulas for the online tuning of k_i and Φ_i with their initial values being set to $k_i(0) = 0$ and $\Phi_i(0) = 0$. In summary, equations 29-31, 34 and 39 determine the control voltage u. In engineering practice, the control system cannot have the capacity to generate infinite voltage, thus the voltage should be restricted to a certain range. The following saturation link is applied to obtain the actual voltage u_a

$$u_a = \begin{cases} u_m & \text{for} \ \ u \ge u_m \\ u & \text{for} \ \ |u| < u_m \\ -u_m & \text{for} \ \ u \le -u_m \end{cases} \tag{40}$$

where u_m is the maximum voltage that can be generated.

B. Delay-Compensated Low-Pass Filter

Executions of dual-layer controllers require the system states z, $\dot{z}$, and I as feedback signals. It is assumed that the displacement z, acceleration $\ddot{z}$, and current I can be measured. The corresponding measurements are denoted as z_m, $\ddot{z}_m$, and I_m, respectively. Sensor noise is assumed to exist in z_m and $\ddot{z}_m$. No noise is assumed to exist in I_m, i.e., $I_m = I$, because the widely used Hall-effect current sensors have good performance in mitigating sensing noise and drift error [36]. In this section, how to obtain the displacement and velocity states based on the measurements z_m, $\ddot{z}_m$ will be presented, where the negative influence of sensor noise can be eliminated as much as possible.

A first-order low-pass filter with the unit gain is applied on z_m to remove the high-frequency noise. The transfer function of the filter is

$$H(s) = \frac{\omega_c}{s + \omega_c} = \frac{1}{1 + \tau s}, \tag{41}$$

where ω_c is the cut-off frequency, and $\tau = 1/\omega_c$ is the approximation to the time delay caused by the filter (a large value of ω_c results in a higher approximation precision).

To compensate for the time delay, the following time-delay compensator is applied after the low-pass filter:

$$G(s) = \exp(\tau s) = \frac{\exp(2\tau s)}{\exp(\tau s)} \approx \frac{1+2\tau s}{1+\tau s}. \tag{42}$$

The low-pass filter and the time-delay compensator together, i.e., $G(s)\cdot H(s)$, form the DCLP filter, which has been proven to cooperate well with the sliding mode controller [37]. The signal processing in this paper is executed in the MATLAB Simulink environment, where $H(s)$ and $G(s)$ can be directly implemented using transfer function blocks. However, a transfer function block in Simulink can only generate the output with zero initial value. Since the initial displacement is not zero, transfer function blocks cannot be used. To address this issue, the transfer function $G(s)\cdot H(s)$ is converted into a state-space representation by using the ss.m function in MATLAB. A state-space block is then adopted, which allows us to type in the initial state value to consider the nonzero initial condition. The state-space representation of $G(s)\cdot H(s)$ is given by

$$\begin{aligned} \dot{\mathbf{x}} &= \mathbf{A}\mathbf{x} + \mathbf{B}z_m \\ z_f &= \mathbf{C}\mathbf{x} + \mathbf{D}z_m \end{aligned} \tag{43}$$

where $\mathbf{x}$ is the 2×1 state vector; $\mathbf{A}$, $\mathbf{B}$, $\mathbf{C}$, and $\mathbf{D}$ are coefficient matrices calculated from the ss.m function; z_f is the filtered displacement, which is the noise-free approximation to z and will be adopted as the control feedback. Assuming that $z_f(0) = z_m(0) = z_0$ and $\dot{z}_f(0) = \dot{z}_m(0) = 0$, where z_0 is the nonzero initial displacement (initial air gap), the following formulas are satisfied:

$$\begin{aligned} z_f(0) &= \mathbf{C}\mathbf{x}(0) + \mathbf{D}z_m(0) = z_0 \\ \dot{z}_f(0) &= \mathbf{C}\dot{\mathbf{x}}(0) = \mathbf{C}\mathbf{A}\mathbf{x}(0) + \mathbf{C}\mathbf{B}z_m(0) = 0 \end{aligned} \tag{44}$$

which yields the initial state value as follows

$$\mathbf{x}(0) = \begin{bmatrix} \mathbf{C} \\ \mathbf{C}\mathbf{A} \end{bmatrix}^{-1} \cdot \begin{bmatrix} z_0 - \mathbf{D}z_0 \\ -\mathbf{C}\mathbf{B}z_0 \end{bmatrix}. \tag{45}$$

The velocity state $\dot{z}$ is calculated by integrating $\ddot{z}_m$. Although noise exists in $\ddot{z}_m$, the integral operation could smooth out the noise to a great extent to make the control system work properly.

C. Forgetting Least-Squares Estimator

Generally speaking, a sliding mode control system with noise rejection is robust to model uncertainties and is adequate for most control problems. However, there is still room for improvement if one can further make the control system adaptive. In this section, the FL estimator will be presented, which cooperates with the dual-layer sliding mode controllers and can enhance the control system with the self-tuning capability to adapt to the plant model variation.

The estimation equation

$$\mathbf{y} = \mathbf{W}\Psi \tag{46}$$

is established for the estimator design, where $\mathbf{y}$ and $\mathbf{W}$ are the vector and matrix formed based on the known signals including command signal and measurements; Ψ is the parameter vector containing all parameters to be estimated. Assuming the *parameter estimation* is $\hat{\Psi}$, the output error is defined as

$$\mathbf{e}_1 = \hat{\mathbf{y}} - \mathbf{y} = \mathbf{W}\hat{\Psi} - \mathbf{W}\Psi = \mathbf{W}\tilde{\Psi} \tag{47}$$

where $\hat{\mathbf{y}} = \mathbf{W}\hat{\Psi}$ is the *predicted output* and $\tilde{\Psi} = \hat{\Psi} - \Psi$ is the *parameter estimation error*, respectively.

A classical least-squares estimator aims to update the parameter estimation instantaneously to minimize

$$J_0(t) = \int_0^t \| \mathbf{e}_1(q) \|^2 \mathrm{d}q \tag{48}$$

where $\| \mathbf{e}_1(q) \|$ is the l^2-norm of $\mathbf{e}_1(q)$. Equation 48 takes into account all the past prediction errors evenly, therefore the estimator has a strong capability to reject the estimation divergence caused by disturbances and measurement noise [18]. However, this feature also leads to the fact that the classical least-squares estimator only works well for estimating constant parameters. To make the estimator able to track time-varying parameters, the weighted sum of the output error squares given by

$$J(t) = \int_0^t \Gamma(q,t) \| \mathbf{e}_1(q) \|^2 \mathrm{d}q \tag{49}$$

is adopted in this paper, where

$$\Gamma(q,t) = \exp\left[-\int_q^t \theta(r)\mathrm{d}r \right] \tag{50}$$

is the *weight coefficient*. $J(t)$ is defined as the *overall output error*. $\Gamma(q,t)$ is positive and increases from $q = 0$ to $q = t$ ($\Gamma(t,t) = 1$), indicating that remote data generated by old parameters have little impact on the overall output error. The rate of increase in $\Gamma(q,t)$ over time is determined by the *forgetting factor* $\theta(r)$. In this way, the estimation of time-varying parameters is achievable.

To minimize $J(t)$, the estimation $\hat{\Psi}$ should satisfy [18]

$$\mathbf{P}(t)^{-1}\hat{\Psi}(t) = \int_0^t \Gamma(q,t)\mathbf{W}^T(q)\mathbf{y}(q)\mathrm{d}q \tag{51}$$

where

$$\mathbf{P}(t)^{-1} = \Gamma(0,t)\mathbf{P}(0)^{-1} + \int_0^t \Gamma(q,t)\mathbf{W}^T(q)\mathbf{W}(q)\mathrm{d}q. \tag{52}$$

$\mathbf{P}(t)$ is defined as the *estimation gain* and $\mathbf{P}(0)^{-1} \neq 0$. By taking the first-order derivative operations on equations 51 and 52, it can deduced that

$$\dot{\hat{\Psi}} = -\mathbf{P}\mathbf{W}^T\mathbf{e}_1, \tag{53}$$

and

$$\frac{\mathrm{d}}{\mathrm{d}t}\left(\mathbf{P}^{-1}\right) = -\theta\mathbf{P}^{-1} + \mathbf{W}^T\mathbf{W}. \tag{54}$$

Since

$$\frac{\mathrm{d}}{\mathrm{d}t}\left(\mathbf{P}\mathbf{P}^{-1}\right) = \dot{\mathbf{P}}\mathbf{P}^{-1} + \mathbf{P}\left[-\theta\mathbf{P}^{-1} + \mathbf{W}^T\mathbf{W}\right] = 0, \tag{55}$$

It can be further obtained that

$$\dot{\mathbf{P}} = \theta\mathbf{P} - \mathbf{P}\mathbf{W}^T\mathbf{W}\mathbf{P}. \tag{56}$$

The forgetting factor θ can be tuned with $\| \mathbf{P}(t) \|$. For simplicity, the constant forgetting factor is used in this paper. A larger θ indicates fast forgetting, which enhances the estimator's ability to capture parameter variations. However, it also leads to more oscillations in the parameter estimations. Therefore, the selection of θ involves a trade-off.

Equations 47, 56 and 53 determine the parameter update law for the FL estimator. The boundedness of the estimation error $\tilde{\Psi}$ and the estimation gain $\mathbf{P}$ can be satisfied (see Ref [38] for the detailed proof), thus the robustness of the FL estimator is guaranteed. The initial value $\mathbf{P}(0)$ needs to be manually assigned based on the available information about the plant model, i.e., prior identified parametric values and their corresponding uncertainly levels. If no information is available, $\mathbf{P}(0)$ can simply be set to a small value such as 0.1, and it will only affect the estimator at the beginning. During the estimation process, $\dot{\mathbf{P}}$ and $\dot{\hat{\Psi}}$ are calculated successively in each time step and then used to update $\mathbf{P}$ and $\hat{\Psi}$ for the next time step.

Regarding the electromagnetic suspension system in this paper, the estimation equation is formed as

$$\underbrace{\ddot{z}_m z_f^2 + \hat{b} I_m^2}_{\mathbf{y}} = \underbrace{z_f^2}_{\mathbf{W}} \cdot \underbrace{a}_{\Psi} \tag{57}$$

according to equation 4 to estimate just one parameter: a based on signals z_f, $\ddot{z}_m$, I_m and the constant parameter $\hat{b}$. The time-varying estimation $\hat{a}$ is then used as the nominal value of a in the first layer sliding mode controller. Instead of estimating both a and b, $b = \hat{b}$ is adopted as a known knowledge to solely estimate a for the following two reasons: 1) based on the same model equation, estimating more parameters will lead to less usable information for estimation compared to estimating just one parameter, therefore it might deliver unsatisfactory results; 2) the variation and uncertainty levels of a and b are different (a is related to train loads which could change greatly, while b is related to the setup of the electromagnet thus b is normally constant or vary in a small range), but only one forgetting factor can be used for all parameters to be estimated in an FL estimator, making it hard to determine the forgetting factor. It is important to point out that $\hat{a}$ does not reflect the real variation of a since $\hat{b}$ is not the true value of b. However, as long as the estimation $\hat{a}$ and the constant $\hat{b}$ can fit the dynamics of equation 4 numerically, it is sufficient for us to make the controller adaptive and improve the control performance.

Finally, the control system SD-SMC is formed with dual-layer sliding mode controllers (SMC1 and SMC2), the DCLP filter, and the FL estimator. The schematic block diagram for the suspension control of the EMS system including these control modules and their interactions in SD-SMC is shown in Fig. 3. To assess the performance of SD-SMC, some numerical examples will be conducted using the MATLAB Simulink package in the following section. The executable Simulink block diagram of SD-SMC is shown in Fig. 4. The "Plant" block functions as a black box to calculate the system's true responses using the uncertain plant model, i.e., equations 1-3, where the exact values of model parameters are unobservable.

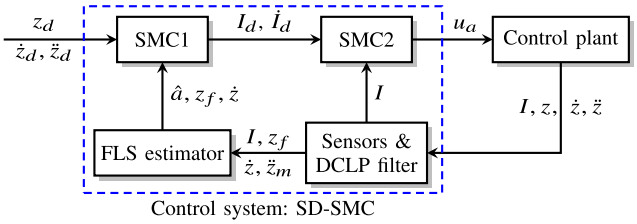

Fig. 3. Schematic block diagram of SD-SMC (SMC1: first layer sliding mode controller; SMC2: second layer sliding mode controller).

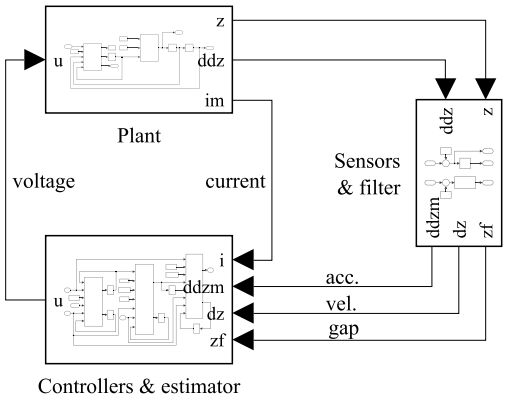

Fig. 4. Executable Simulink block diagram of SD-SMC.

TABLE I
PARAMETRIC VALUES OF THE EMS SYSTEM

m (kg)	N_e (unitless)	A_e (m^2)	R (Ω)
700	450	0.024 ± 0.0024	1.2 ± 0.12

μ_0 ($N{\cdot}A^{-2}$)	$F(t)$ (N)	u_m (V)
$4\pi \times 10^{-7}$	27440 ± 5488	400

Band-limited white noises (BLWN) are added to the system's true displacement and acceleration responses to mimic the noised measurements z_m and $\ddot{z}_m$.

IV. NUMERICAL EXAMPLES

A. Simulation Setup

For EMS medium- or low-speed maglev trains, the security requirement is $z_d = 8$mm [39]. The initial air gap is assumed to be $z_0 = 16$mm. The parametric values of the EMS system are listed in Table I, where A_e, R, and $F(0)$ are randomly selected constants ranging in $\pm 10\%$, $\pm 10\%$ and $\pm 20\%$ of their nominal values (0.024m^2, 1.2Ω, and $4mg = 27440$N). Different variations of $F(t)$ will be considered in numerical examples to access the control system.

Based on Table I, the nominal parametric values and their corresponding error boundaries of the control plants for dual-layer sliding mode controllers and FL estimator can be obtained, as listed in Table II. The nominal value $\hat{a}(t)$ is different from the other three nominal values $\hat{b}$, $\hat{R}$, and $\hat{C}$ which are constants because $\hat{a}(t)$ is updated in every time step by the FL estimator, and $\hat{a}(0) = \hat{F}(0)/m = 4mg/m = 4g = 39.2\text{m}{\cdot}\text{s}^{-2}$. A wide and tunable boundary $\bar{a}(t) = 0.2\hat{a}(t)$ is adopted as the error boundary of $\hat{a}(t)$. The power spectral densities of the sensor self-noise for displacement and

TABLE II
NOMINAL PARAMETRIC VALUES AND THEIR ERROR BOUNDARIES OF THE CONTROL PLANTS

SMC1 & FL estimator			
$\hat{a}(0)$ (m·s^{-2})	$\bar{a}(t)$ (m·s^{-2})	$\hat{b}$ (m^3·s^{-2}·A^{-2})	$\bar{b}$ (m^3·s^{-2}·A^{-2})
39.2	$0.2\hat{a}(t)$	2.1812×10^{-5}	2.1812×10^{-6}
SMC2			
$\hat{R}$ (Ω)	$\bar{R}$ (Ω)	$\hat{C}$ (N·m^2·A^{-2})	$\bar{C}$ (N·m^2·A^{-2})
1.2	0.12	1.5268×10^{-2}	1.5268×10^{-3}

TABLE III
VALUES OF SD-SMC CONTROL PARAMETERS

SMC1		SMC2		FL estimator		DCLP filter
λ_z, f_z	η_z	f_i	η_i	θ	$\mathbf{P}(0)$	τ
200 or 100	0.1	100	0.1	200	0.1	0.01

acceleration measurements are set to 2.56×10^{-10}m^2, and 2.16×10^{-5}m^2·s^{-4}, by referring to [35] and [40], respectively.

The fixed-step fourth-order Runge-Kutta solver (ODE4) is adopted for the Simulink program, and the sampling time step is set to 0.001s. Values of the control parameters for the control system are listed in Table III. The control system performance is most sensitive to λ_z and f_z, moderately sensitive to f_i and θ, and slightly sensitive to η_z, η_i, $\mathbf{P}(0)$, and τ. It has been tested that η_z, η_i and $\mathbf{P}(0)$ can be set to small values from 10^{-10} to 0.2, and τ can be set to five to ten times of the sampling time step. Values of the other parameters are determined with caution by trying different values and comparing the corresponding control performance. It should be noted that values of the control parameters listed in Table III are obtained only after a few trials and they might not be the optimum values. The authors acknowledge that, to the best of their knowledge, there is currently no systematic procedure to determine the optimum values for the control parameters. However, using these values is sufficient to achieve satisfactory control performance. Two cases: $\lambda_z = f_z = 200$ and $\lambda_z = f_z = 100$ will be investigated and other control parameters will be fixed in the numerical examples.

As mentioned above, dual-layer sliding mode controllers might work without using boundary layers. However, in this case, the control system will be very aggressive, and it could excite a high level of chattering in the system response. Simulation results indicate that the control system tends to be unstable when boundary layers are not adopted. The command voltage should be limited within $\pm$400V by performing the command saturation operation. The voltage limit can be easily reached at the very beginning when the control system tries to generate a large command to drive the gap value to the designated value. Reaching the voltage limit consumes more power and even leads to the failure of the control system, thus should be avoided. Both boundary layers and command saturation are adopted in this paper.

B. Simulation Results

The effectiveness of the FL estimator, comparisons with another controller, and the control strategy optimization are studied successively.

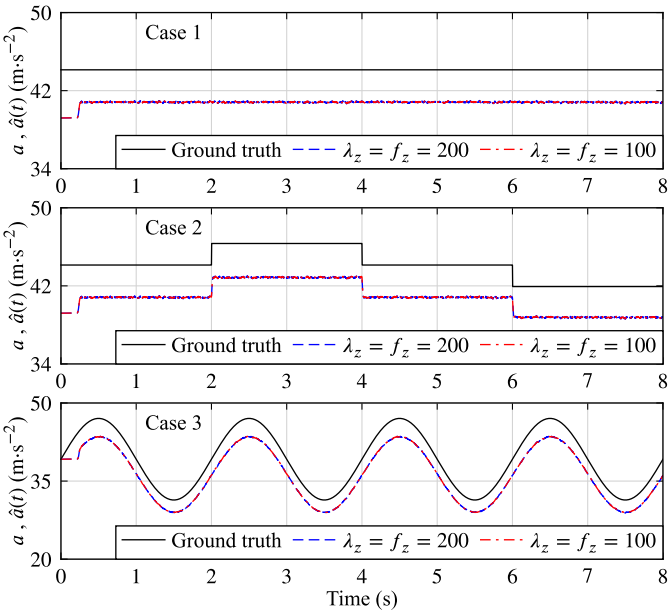

Fig. 5. Time histories of the parameter a and its estimation $\hat{a}(t)$ for three cases.

1) Effectiveness of the FL Estimator: Three cases are investigated in this section. For Case 1, the parameter a is assumed to be a fixed random value in 39.2 ± 7.84. For the other two cases, a is not a constant value. The three cases of a are plotted using solid lines in Fig. 5.

The parameter estimation results ($\lambda_z = f_z = 100$ and $\lambda_z = f_z = 200$) generated from the FL estimator for the three cases are also plotted in Fig. 5. It can be observed that the FL estimator starts to work after 0.2s and can track the parameter variations quite well since then. It is remarked here that drifts exist between the estimations and the ground true values shown in Fig. 5. The reason is that the other parameter ($\hat{b}$) used in the FL estimator is not the true parameter value of the control plant. As discussed previously, since the estimations can mathematically fit the control plant, the performance of SD-SMC is not affected by the drifts.

The gap signals of the suspension system with and without estimators for the three cases are plotted in Figs. 6 to 8, where the results for $\lambda_z = f_z = 200$ and $\lambda_z = f_z = 100$ are compared. Note that the gap ranges in these figures are zoomed around 8mm to display the differences more intuitively. If the FL estimator is not adopted, larger λ_z and f_z values can enhance the gap stabilization capability of the control system, but at the price of causing higher command voltages (see Fig. 9 for Case 3). Decreasing λ_z and f_z values could mitigate this issue, while the gap stabilization performance deteriorates greatly when the FL estimator is not used, especially for Case 3. However, implementing the FL estimator allows the adoption of smaller values for λ_z and f_z to reduce the command voltage without degrading the control performance. The FL estimator with parameters $\lambda_z = f_z = 100$ will be adopted for numerical examples in this paper unless otherwise specified.

2) Comparison With the Linear Approximation Controller: This section compares the proposed SD-SMC with the linear

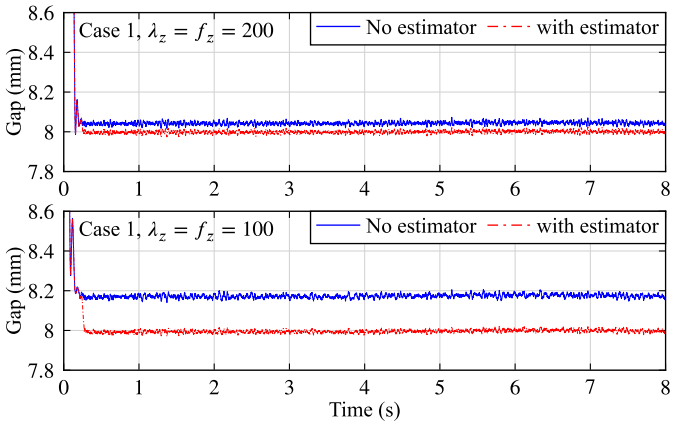

Fig. 6. Time histories of the suspension gap with and without the FL estimator for Case 1.

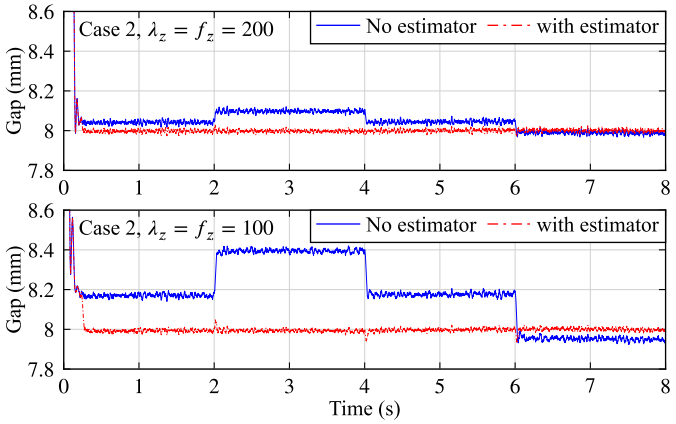

Fig. 7. Time histories of the suspension gap with and without the FL estimator for Case 2.

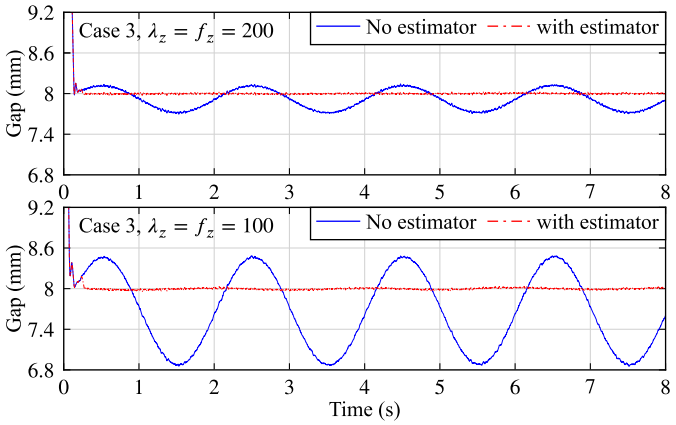

Fig. 8. Time histories of the suspension gap with and without the FL estimator for Case 3.

approximation controller (LAC) where the nonlinear suspension system is linearized using the two-dimensional Taylor expansion. The suspension force f_e can be linearized at the equilibrium points I_d and z_d as

$$f_e(I,z) = C\frac{I^2}{z^2} \approx f_e(I_d,z_d) + \left.\frac{\partial f_e}{\partial I}\right|_{I_d,z_d} + \left.\frac{\partial f_e}{\partial z}\right|_{I_d,z_d} = \frac{\hat{C}I_d^2}{z_d^2} + \frac{2\hat{C}I_d}{z_d^2}I - \frac{2\hat{C}I_d^2}{z_d^3}z \tag{58}$$

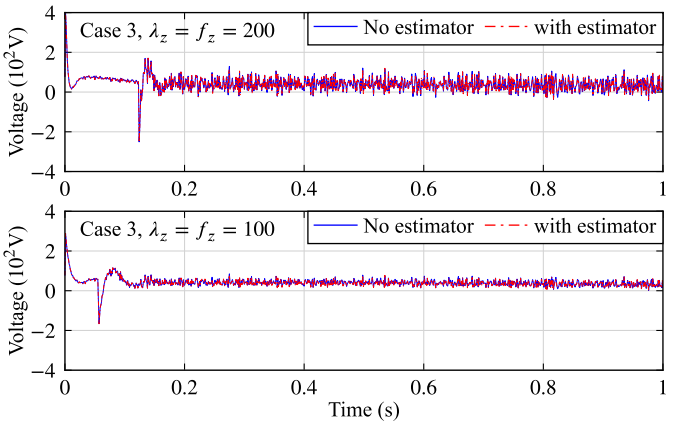

Fig. 9. Time histories of the command voltage with and without the FL estimator for Case 3 (first one second).

where

$$z_d = 8\text{mm},\ \ I_d = \sqrt{\hat{F}(0)z_d^2/\hat{C}} = 33.91\text{A}. \tag{59}$$

Note that I_d is not the true equilibrium point but the nominal equilibrium point because the above calculation uses nominal parametric values of the system. According to equation 2 and 58, $\ddot{z}$ can be approximated to

$$\ddot{z} = \frac{F}{m} - \frac{f_e(I,z)}{m} \approx \frac{2\hat{C}I_d^2}{mz_d^3}z - \frac{2\hat{C}I_d}{mz_d^2}I. \tag{60}$$

The LAC command is designed as

$$u = k_1(z - z_d) + k_2\dot{z} + k_3 I. \tag{61}$$

Equation 3 can be approximated to

$$u = \hat{R}I + \frac{2\hat{C}}{z}\dot{I} - \frac{2\hat{C}I}{z^2}\dot{z} \tag{62}$$

Combining equations 60-62 to eliminate u and I results in the transfer function $G_z(s)$ between z_d and z as follows

$$G_z(s) = \frac{Z(s)}{Z_d(s)} = \frac{\beta_4}{s^3 + \beta_1 s^2 + \beta_2 s + \beta_3} \tag{63}$$

where

$$\beta_1 = (\hat{R} - k_3)\frac{z_d}{2\hat{C}},\ \ \beta_2 = \frac{k_2 I_d}{mz_d},$$
$$\beta_3 = (k_3 - \hat{R})\frac{I_d^2}{mz_d^2} + \frac{k_1 I_d}{mz_d},\ \ \beta_4 = \frac{k_1 I_d}{mz_d}. \tag{64}$$

If $G_z(s)$ can be written as

$$G_z(s) = \frac{\gamma_0\gamma\xi\omega_n}{(s^2 + 2\xi\omega_n + \omega_n^2)(s + \gamma\xi\omega_n)} \tag{65}$$

where $0.99 \geq \xi \geq 0.05$, $\omega_n > 0$, and γ is no less than a specific positive value depending on the value of ξ [41], the third-order system $G_z(s)$ can be reduced to a second-order system

$$G_z'(s) = \frac{\gamma_0}{s^2 + 2\xi\omega_n + \omega_n^2} \tag{66}$$

within around 10% normalized errors regarding the settling time and maximum overshoot in the step response. For the

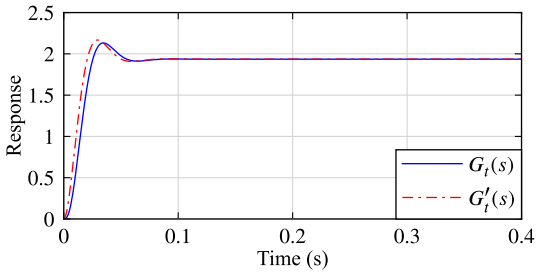

Fig. 10. Unit step responses of the original third-order system $G_t(s)$ and the reduced second-order system $G'_t(s)$.

second-order system $G'_z(s)$, approximation formulas within the 2% error band to calculate the settling time t_s and the maximum overshoot M_o are

$$t_s \approx \frac{4}{\xi\omega_n}, \quad M_o \approx \exp\left(-\frac{\xi\pi}{\sqrt{1-\xi^2}}\right) \times 100\%. \tag{67}$$

By setting $\gamma = 3.6$, $t_s = 0.056$s, $M_o = 12\%$ (a high overshot is set here to compensate for the model error of the linear approximation at the initial stage of control), it can be calculated from equation 67 that $\xi = 55.9\%$ and $\omega_n = 127.7$Hz, therefore, $(s^2 + 2\xi\omega_n + \omega_n^2)(s + \gamma\xi\omega_n)$ yields

$$s^3 + 400s^2 + 5.30 \times 10^4 s + 4.19 \times 10^6, \tag{68}$$

i.e., $\beta_1 = 400$, $\beta_2 = 5.30 \times 10^4$, $\beta_3 = 4.19 \times 10^6$. According to equation 64, $\beta_4 = 8.11 \times 10^6$ and the control parameters of the LAC command: $k_1 = 1.34 \times 10^6$, $k_2 = 8.75 \times 10^3$, and $k_3 = -1.51 \times 10^2$ can be obtained. Fig. 10 shows that the unit step responses of $G_z(s)$ and $G'_z(s)$ are close to each other, therefore, the above procedure to determine the control parameters of LAC based on the reduced system is acceptable.

Because the steady-state response of $G_t(s)$ shown in Fig. 10 is not unity, there will be a steady-state error between z and z_d using the control law (equation 61). To eliminate steady-state error, an integral control term can be added to the control command. Furthermore, z is unavailable and is replaced by the filtered measurement z_f in the control command. Finally, the LAC control command is revised to

$$u_l = k_1(z_f - z_d) + k_2\dot{z} + k_3 I + k_I \int (z_f - z_d)\mathrm{d}t, \tag{69}$$

where the last term is the integral control term, and k_I is set to 1×10^7 after trial and error.

The gap signals of the suspension system for the three cases using LAC and SD-SMC are plotted in Fig. 11. The root mean square (RMS) and maximum errors of gap stabilizations in 1-8s of three cases under two control systems are listed in Table IV, where numbers in parentheses are decreased (negative values) or increased (positive value) percentages of errors of SD-SMC compared to the corresponding errors of LAC. Compared to SD-SMC, LAC results in closed times to reach the target gap, however, it generates larger gap fluctuations and errors for Cases 2 and 3 where parameter variations are introduced. Additionally, the voltage level of LAC is higher than that of SD-SMC (see Fig. 12 for Case 3). It's worth noting that the control parameters of LAC have been tuned to optimal to the best of the authors' knowledge, while

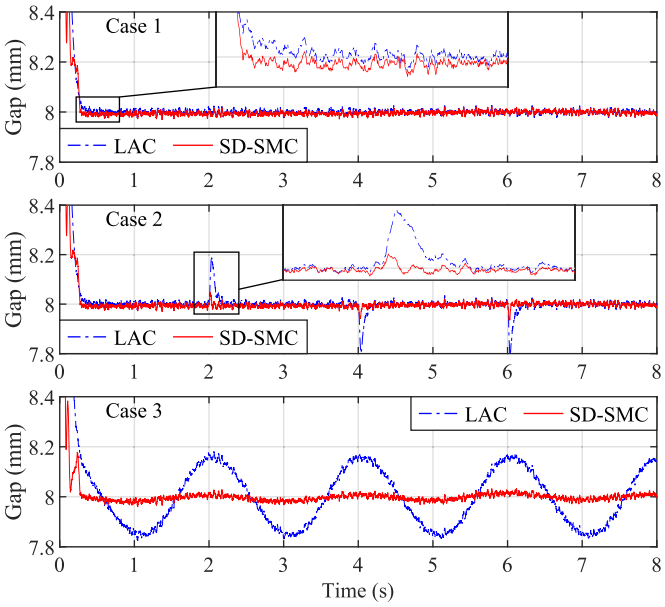

Fig. 11. Time histories of the suspension gap using LAC and SD-SMC ($\lambda_z = f_z = 100$).

TABLE IV
RMS AND MAXIMUM ERRORS OF GAP STABILIZATIONS IN 1-8S OF NUMERICAL CASES UNDER LAC AND SD-SMC

Case no.	RMS errors (mm)		Maximum errors (mm)	
	LAC	SD-SMC	LAC	SD-SMC
1	0.0083	0.0081 (−2.5%)	0.0349	0.0305 (−12.7%)
2	0.0272	0.0096 (−64.6%)	0.2066	0.0646 (−68.7%)
3	0.1103	0.0118 (−89.3%)	0.1819	0.0399 (−78.1%)

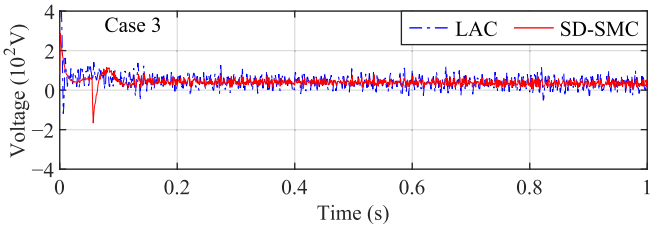

Fig. 12. Time histories of the command voltage signals for Case 3 using LAC and SD-SMC ($\lambda_z = f_z = 100$).

it is still incompetent to mitigate the large gap fluctuations and higher voltages.

3) Control Strategy Optimization: In previous sections, the designated motions of the suspension system are set to

$$z_d = 8\text{mm}, \ \dot{z}_d = 0, \ \ddot{z}_d = 0. \tag{70}$$

This control strategy is referred as to the *instant-suspension strategy* in this paper. However, the sudden change of the gap from $z_0 = 16$mm to $z_d = 8$mm causes high velocity and acceleration oscillations. To make a smooth gap change, the designated motions can be modified as follows

$$z'_d = \begin{cases} \dfrac{A}{\omega^2}\sin(\omega t) - \dfrac{A}{\omega}t + z_0 \ \text{for} \ t \le t_d \\ z_d \ \text{for} \ t > t_d, \end{cases} \tag{71}$$

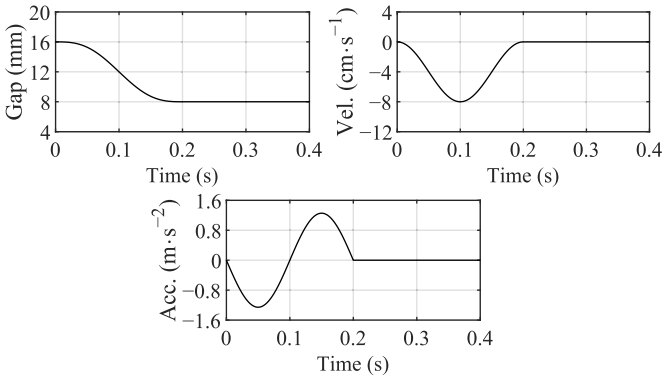

Fig. 13. Modified designated motions of the suspension system ($t_d = 0.2$s).

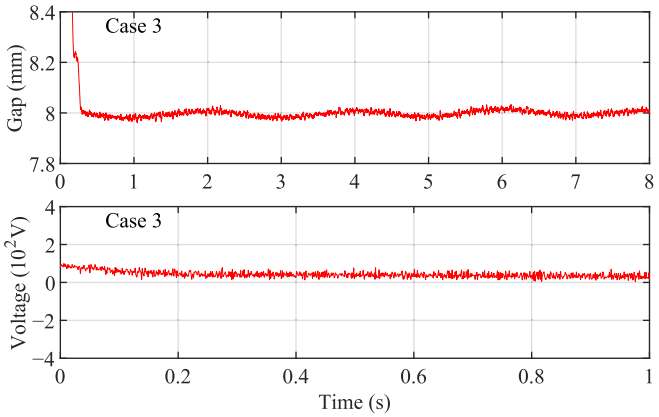

Fig. 14. Time histories of the suspension gap and command voltage for Case 3 under the smooth-suspension strategy ($\lambda_z = f_z = 100$, $t_d = 0.2$s).

$$\dot{z}_d' = \begin{cases} \frac{A}{\omega}\cos(\omega t) - \frac{A}{\omega} \text{ for } t \le t_d \\ 0 \text{ for } t > t_d, \end{cases} \tag{72}$$

$$\ddot{z}_d' = \begin{cases} -A\sin(\omega t) \text{ for } t \le t_d \\ 0 \text{ for } t > t_d, \end{cases} \tag{73}$$

where

$$A = \frac{2\pi(z_0 - z_d)}{t_d^2}, \ \omega = \frac{2\pi}{t_d}, \tag{74}$$

and t_d is the reach time, i.e., the time when z_d is expected to be reached. By setting $t_d = 0.2$s, the modified designated motions of the suspension system are plotted in Fig. 13.

When the modified designated motions, i.e., equations 71, 72, 73, are used instead of the sudden-change designated motions, i.e, equation 70, the control system will work more smoothly during the gap control process. This control strategy is referred as to the *smooth-suspension strategy* in this paper. For a demonstration, the gap and command voltage signals of the suspension system for Case 3 under the smooth-suspension strategy are plotted in Fig. 14, where the command voltage is decreased to a large extent, while the gap is still stabilized at around 0.2s. The above simulation results indicate that adopting boundary layers, the FL estimator, and the smooth-suspension strategy can make the control system achieve a good control performance with gentle and low-level control voltages.

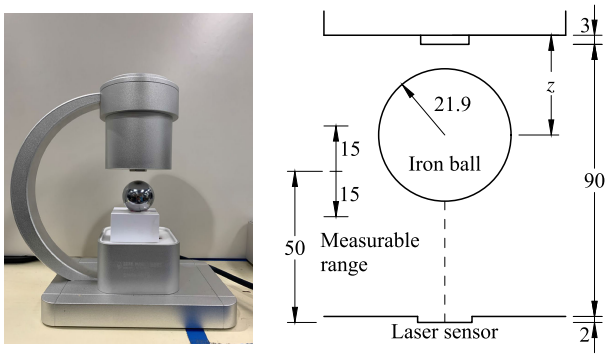

Fig. 15. Side view of the electromagnetic suspension body (left) and main dimensions (right, unit: mm).

V. Experimental Examples

A. Experimental Setup

Real-time control experiments are carried out in this section. The electromagnetic suspension system used for experiments is GML2001(V2018A) manufactured by Googol Technology (Hong Kong) Limited, as shown in Fig. 15. The ODE4 solver is adopted for the Simulink program, and the simulation time interval is 0.003s. Recorded videos of experiments can be found in the online folder: Videos.

A laser displacement sensor is embedded at the bottom of the electromagnetic suspension body. The laser sensor can measure the distance varying in 50 ± 15mm, as depicted in Fig. 15. The electromagnetic core cannot attract the iron ball when the gap z exceeds 45mm. To make the iron ball location always measurable, protect the device, and ensure that the iron ball can be lifted from its initial position by the attractive force, a 3D-printed plastic block (height: 35mm) which allows the laser to travel through is glued on the platform of the electromagnetic suspension body, and the iron ball is placed on the top of the plastic block as the initial state during experiments. The output of the laser sensor is the voltage V_l (≤ 5V). After a series of calibration experiments (omitted here for readability), the relationship between the gap z (unit: mm) and the laser voltage V_l (unit: V) is found to be linear, expressed as

$$z = 5.9391 V_l + 14.7735. \tag{75}$$

According to the parametric values listed in Table V, the effective polar area of the electromagnetic coil is

$$A_e = \pi \times (22/2 + 0.8)^2 = 437.435\text{mm}^2, \tag{76}$$

the nominal value of C is

$$\hat{C} = \mu_0 A_e N_e^2/4 = 8.249 \times 10^{-4}\text{N}\cdot\text{m}^2\cdot\text{A}^{-2}, \tag{77}$$

and the nominal value of the external force is $\hat{F}(0) = mg = 1.0143$N. Same as the numerical examples, the error boundaries of $b = C/m$ and $a(t) = F(t)/m$ are assumed to be $\pm 10\%$ of $\hat{b} = \hat{C}/m$ and $\pm 20\%$ of the estimation $\hat{a}(t)$, see Table VI.

Two remarks are noted here. The first remark is that the second layer controller (SMC2) involving the conversion from the current command I_d to the coil voltage command u does

TABLE V
PARAMETRIC VALUES OF THE ELECTROMAGNETIC SUSPENSION BODY AND THE IRON BALL

Ball mass	Coil turns	Core diameter	Enamelled wire diameter
103.5g	2450	21.9mm	0.8mm

TABLE VI
NOMINAL PARAMETRIC VALUES AND THEIR ERROR BOUNDARIES FOR THE CONTROL EXPERIMENTS

SMC1 & FL estimator			
$\hat{a}(0)$ (m·s^{-2})	$\bar{a}(t)$ (m·s^{-2})	$\hat{b}$ (m^3·s^{-2}·A^{-2})	$\bar{b}$ (m^3·s^{-2}·A^{-2})
9.8	$0.2\hat{a}(t)$	7.970×10^{-4}	7.970×10^{-5}

TABLE VII
VALUES OF S-SMC CONTROL PARAMETERS FOR EXPERIMENTS

SMC1			FL estimator	
λ_z	f_z	η_z	θ	$\mathbf{P}(0)$
20	10	0.1	10	0.1

not apply to the control experiments in this paper because a power amplifier that directly converts current to voltage is installed in the device. The dynamics and time lags caused by the power amplifier can be ignored, thus a static coil current-voltage mapping relationship can be formed. A 2nd-degree polynomial is found to perform well in fitting the current-voltage mapping relationship, given by

$$u = 20.71I_d^2 - 37.52I_d + 17.40. \tag{78}$$

Note that the coil current of the device is not measurable and the calculation of current does not consider model uncertainties, therefore equation 78 might be considerably different from the true current-voltage relationship. However, the proposed control system can compensate for such differences caused by model uncertainties. A voltage saturation link is also adopted to ensure that the actual voltage command does not exceed ±10V. Since there is no second layer controller, the abbreviation S-SMC (i.e., self-tuning sliding mode control system) is used for experimental examples.

The second remark is that the iron ball acceleration cannot be measured during experiments. The ball velocity and acceleration are obtained by taking the first and second derivatives of the gap. Although errors will be enlarged by derivative operations and might drive the system unstable, the proposed control system still works properly because the laser displacement sensor has high precision and can keep errors in small ranges. Values of S-SMC control parameters for experiments are determined by trial and error, which are listed in Table VII.

B. Experimental Results

S-SMC is compared to the demo PID for several experimental cases in this section. The control law of the demo PID directly takes voltages as input and output, given by

$$u_{\text{pid}} = K_p e_l + K_i \int e_l \mathrm{d}t + K_d \dot{e}_l + u_0, \tag{79}$$

TABLE VIII
VALUES OF PID CONTROL PARAMETERS

Case no.	Target gap (mm)	PID control parameters			
		K_i	K_i	K_d	u_0 (V)
1, 4	30	2.9	0.0015	38	0.8
2, 5	33	5.5	0.0051	72	1.7
3, 6	36	8.1	0.019	122	3

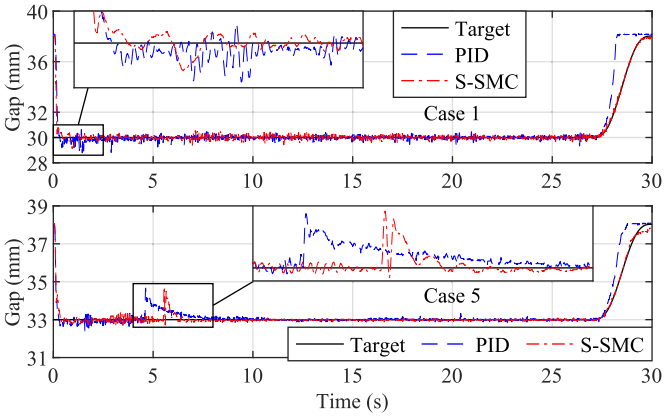

Fig. 16. Target and measured time histories of the ball suspension gap for Cases 1 and 5.

where u_{pid} is the control coil voltage of PID; $e_l = V_l - V_{ld}$, V_{ld} is the target laser voltage calculated from the target gap z_d using equation 75; K_p, K_i, and K_d and the PID control parameters; u_0 is the steady coil voltage, which would make PID perform better if it is set to the output voltage when the iron ball keeps stable at the target position.

Three normal cases where the target gaps are 30mm, 33mm, and 36mm are selected for experiments. A roll of tape weighing $m_t = 16.2$g is used to create another three disturbance cases (Cases 4-6) corresponding to Cases 1-3 by dropping it on the iron ball at around 6s. The optimal values of PID control parameters for these cases obtained by trial and error are listed in Table VIII. The time duration is 30s. To make the ball drop gently at the end of each test, a smooth transaction from the target gap to the initial gap is created in the target gap trajectory at the last three seconds (27)-30s).

The gap stabilization results of S-SMC and PID for Cases 1 and 5 are plotted in Fig. 16 for demonstration. It can be seen from the zoomed plots that S-SMC can generate oscillations with lower amplitudes and frequencies than PID. For the disturbance cases, although the sudden gap drifts caused by the disturbance under S-SMC and PID are close, S-SMC takes less time to restore the gap to the target value.

The RMS and maximum errors of gap stabilization in 1-25s of Cases 1-6 under S-SMC and PID are listed in Table IX, where numbers in parentheses are decreased (negative values) or increased (positive value) percentages of errors of S-SMC compared to the corresponding errors of PID. It is observed that S-SMC achieves much lower errors than PID in most cases, except for maximum errors in Cases 4 and 5. In conclusion, S-SMC outperforms PID in the gap stabilization experiments.

TABLE IX
RMS AND MAXIMUM ERRORS OF GAP STABILIZATIONS IN 1-25S OF EXPERIMENTAL CASES UNDER PID AND S-SMC

Case no.	RMS errors (mm)		Maximum errors (mm)	
	PID	S-SMC	PID	S-SMC
1	0.1711	0.1515 (−11.5%)	1.2197	0.6977 (−42.8%)
2	0.2028	0.0949 (−53.2%)	1.3488	0.5072 (−62.4%)
3	0.1340	0.0707 (−47.2%)	0.8131	0.2911 (−64.2%)
4	0.2941	0.1749 (−40.5%)	1.7454	1.9412 (11.2%)
5	0.2041	0.1371 (−32.8%)	1.6645	1.7411 (4.6%)
6	0.1644	0.1326 (−19.3%)	1.5091	1.1611 (−23.1%)

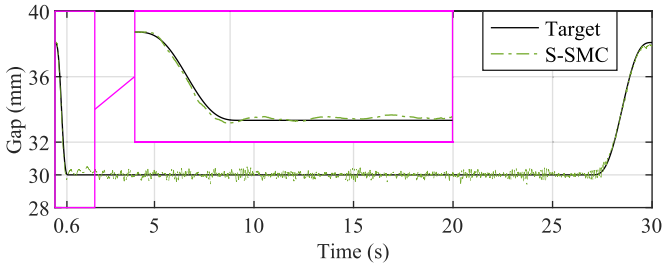

Fig. 17. Target and measured time histories of the ball suspension gap for Case 1 (S-SMC, smooth-suspension strategy, $t_d = 0.6$s).

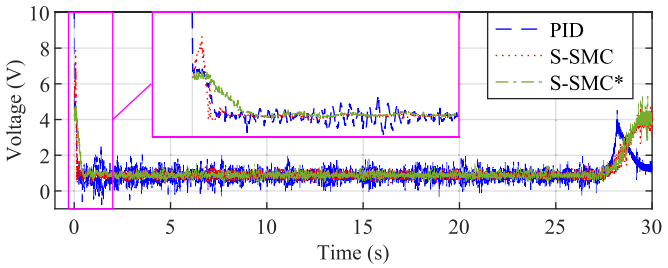

Fig. 18. Command voltage signals for Case 1 using different control systems (PID and S-SMC use the instant-suspension strategy; S-SMC* uses the smooth-suspension strategy).

The smooth-suspension strategy proposed for SD-SMC in numerical examples can be also adopted for S-SMC in experimental examples. It has been tested that the smooth-suspension strategy does not work for PID. Fig. 17 shows the gap smooth-suspension result for Case 1 using S-SMC (the reach time is set to $t_d = 0.6$s), where good gap tracking performance is obtained. The corresponding coil voltage result under S-SMC using the smooth-suspension strategy (labeled as S-SMC* in Fig. 18) is compared with the voltage results under PID and S-SMC using the instant-suspension strategy in Fig. 18. PID generates the voltage with a large initial value that reaches the voltage limit (10V) and a larger varying range than S-SMC and S-SMC*. The voltage leap at the beginning is effectively eliminated by S-SMC*.

VI. CONCLUSION

This paper presents a novel robust and adaptive control system SD-SMC that includes dual-layer sliding mode controllers, a DCLP filter, and an FL estimator for the air gap stabilization problem of the suspension system in EMS trains, where model uncertainties, sensor noise, voltage saturation, and force variations are considered. The first layer sliding mode controller is used to obtain the designated current trajectory which can stabilize the air gap, and then the second layer sliding mode controller is implemented to generate the command voltage to track the current trajectory. Both controllers are designed to be robust to model uncertainties, and the FL estimator is adopted to tune the first layer controller to further make the control system adaptive. Additionally, a DCLP filter is included in SD-SMC to reject sensor noise.

Both numerical and experimental examples are studied. Results of numerical examples indicate that the FL estimator can reduce the command voltages, mitigate the overshooting issue, and loosen restrictions on the control parameters. Comparisons between SD-SMC and LAC show that SD-SMC outperforms LAC. Additionally, the smooth-suspension strategy is proposed where the stabilization problem is converted to the tracking problem, which can further reduce the command voltages at the initial stage. Then, iron ball suspension experiments are conducted to assess the performance of the proposed control system, where the second layer controller is not implemented due to the device configuration. Experimental results reveal that the proposed control system achieves higher and more stable performance than PID. In the follow-up work, in-depth experimental studies are expected to be conducted to investigate SD-SMC for large-scale suspension systems.

REFERENCES

[1] H.-W. Lee, K.-C. Kim, and J. Lee, "Review of maglev train technologies," *IEEE Trans. Magn.*, vol. 42, no. 7, pp. 1917–1925, Jul. 2006.
[2] Y. Xu, Z. Long, Z. Zhao, M. Zhai, and Z. Wang, "Real-time stability performance monitoring and evaluation of maglev trains' levitation system: A data-driven approach," *IEEE Trans. Intell. Transp. Syst.*, vol. 23, no. 3, pp. 1912–1923, Mar. 2022.
[3] Z. Deng et al., "A high-temperature superconducting maglev-evacuated tube transport (HTS maglev-ETT) test system," *IEEE Trans. Appl. Supercond.*, vol. 27, no. 6, pp. 1–8, Sep. 2017.
[4] Y. Sun, Z. He, J. Xu, W. Sun, and G. Lin, "Dynamic analysis and vibration control for a maglev vehicle-guideway coupling system with experimental verification," *Mech. Syst. Signal Process.*, vol. 188, Apr. 2023, Art. no. 109954.
[5] M. Li, X. Chen, S. Luo, W. Ma, and D. Gao, "Analysis on abnormal low-frequency vertical vibration of medium-low-speed maglev vehicle," *Mech. Syst. Signal Process.*, vol. 200, Oct. 2023, Art. no. 110510.
[6] X. Wang and J. Huang, "Study on electromagnetic relationship and dynamic characteristics of superconducting electrodynamic maglev train on curved track," *IEEE Trans. Intell. Transp. Syst.*, vol. 24, no. 6, pp. 6146–6164, Feb. 2023.
[7] Z. Liu, Z. Long, and X. Li, "Maglev train overview," in *Maglev Trains: Key Underlying Technologies*. Berlin, Germany: Springer, 2015, ch. 1, pp. 1–28. [Online]. Available: https://link.springer.com/content/pdf/10.1007/978-3-662-45673-6.pdf
[8] R.-J. Wai, J.-D. Lee, and K.-L. Chuang, "Real-time PID control strategy for maglev transportation system via particle swarm optimization," *IEEE Trans. Ind. Electron.*, vol. 58, no. 2, pp. 629–646, Feb. 2011.
[9] A. Ghosh, T. Rakesh Krishnan, P. Tejaswy, A. Mandal, J. K. Pradhan, and S. Ranasingh, "Design and implementation of a 2-DOF PID compensation for magnetic levitation systems," *ISA Trans.*, vol. 53, no. 4, pp. 1216–1222, Jul. 2014.
[10] D. Maji, M. Biswas, A. Bhattacharya, G. Sarkar, T. K. Mondal, and I. Dey, "MAGLEV system modeling and LQR controller design in real time simulation," in *Proc. Int. Conf. Wireless Commun., Signal Process. Netw. (WiSPNET)*, Mar. 2016, pp. 1562–1567.
[11] M. Khan, A. S. Siddiqui, and A. S. A. Mahmoud, "Robust H_∞ control of magnetic levitation system based on parallel distributed compensator," *Ain Shams Eng. J.*, vol. 9, no. 4, pp. 1119–1129, Dec. 2018.

[12] Y. Sun, J. Xu, H. Wu, G. Lin, and S. Mumtaz, "Deep learning based semi-supervised control for vertical security of maglev vehicle with guaranteed bounded airgap," *IEEE Trans. Intell. Transp. Syst.*, vol. 22, no. 7, pp. 4431–4442, Jul. 2021.

[13] Q. Chen, Y. Tan, J. Li, D. Oetomo, and I. Mareels, "Model-guided data-driven decentralized control for magnetic levitation systems," *IEEE Access*, vol. 6, pp. 43546–43562, 2018.

[14] Q. Chen et al., "Decentralized control design and implementation for magnetic levitation systems with extended state observer," *Control Theory Technol.*, vol. 21, no. 3, pp. 397–413, Sep. 2023.

[15] G. He, J. Li, and P. Cui, "Nonlinear control scheme for the levitation module of maglev train," *J. Dyn. Syst., Meas., Control*, vol. 138, no. 7, Jul. 2016, Art. no. 074503.

[16] N. Sahoo, A. Tripathy, and P. Sharma, "Single axis control of ball position in magnetic levitation system using fuzzy logic control," *IOP Conf. Ser., Mater. Sci. Eng.*, vol. 323, Mar. 2018, Art. no. 012020.

[17] J. Zhang, X. Wang, and X. Shao, "Design and real-time implementation of Takagi–Sugeno fuzzy controller for magnetic levitation ball system," *IEEE Access*, vol. 8, pp. 38221–38228, 2020.

[18] J.-J. E. Slotine and W. Li, "Sliding mode control," in *Applied Nonlinear Control*. Englewood Cliffs, NJ, USA: Prentice-Hall, 1991, ch. 7, pp. 276–310. [Online]. Available: https://lewisgroup.uta.edu/ee5323/notes/Slotine

[19] H.-W. Li, F. Wang, Y.-Q. Ni, Y.-W. Wang, and Z.-D. Xu, "An adaptive and robust control strategy for real-time hybrid simulation," *Sensors*, vol. 22, no. 17, p. 6569, Aug. 2022.

[20] C. S. Chin and C. Wheeler, "Sliding-mode control of an electromagnetic actuated conveyance system using contactless sensing," *IEEE Trans. Ind. Electron.*, vol. 60, no. 11, pp. 5315–5324, Nov. 2013.

[21] J. Pan, W. Li, and H. Zhang, "Control algorithms of magnetic suspension systems based on the improved double exponential reaching law of sliding mode control," *Int. J. Control, Autom. Syst.*, vol. 16, no. 6, pp. 2878–2887, Nov. 2018.

[22] S. Wan, X. Li, W. Su, J. Yuan, and J. Hong, "Active chatter suppression for milling process with sliding mode control and electromagnetic actuator," *Mech. Syst. Signal Process.*, vol. 136, Feb. 2020, Art. no. 106528.

[23] J. Gil, S. You, Y. Lee, and W. Kim, "Nonlinear sliding mode controller using disturbance observer for permanent magnet synchronous motors under disturbance," *Expert Syst. Appl.*, vol. 214, Mar. 2023, Art. no. 119085.

[24] C. Edwards and Y. B. Shtessel, "Adaptive continuous higher order sliding mode control," *Automatica*, vol. 65, pp. 183–190, Mar. 2016.

[25] N. K. Sharma, S. Roy, S. Janardhanan, and I. N. Kar, "Adaptive discrete-time higher order sliding mode," *IEEE Trans. Circuits Syst. II, Exp. Briefs*, vol. 66, no. 4, pp. 612–616, Apr. 2019.

[26] S. Roy, S. Baldi, and L. M. Fridman, "On adaptive sliding mode control without *a priori* bounded uncertainty," *Automatica*, vol. 111, Jan. 2020, Art. no. 108650.

[27] X. Su, Y. Xu, and X. Yang, "Neural network adaptive sliding mode control without overestimation for a maglev system," *Mech. Syst. Signal Process.*, vol. 168, Apr. 2022, Art. no. 108661.

[28] H. M. S. Yaseen, S. A. Siffat, I. Ahmad, and A. S. Malik, "Nonlinear adaptive control of magnetic levitation system using terminal sliding mode and integral backstepping sliding mode controllers," *ISA Trans.*, vol. 126, pp. 121–133, Jul. 2022.

[29] H. M. M. Adil, S. Ahmed, and I. Ahmad, "Control of MagLev system using supertwisting and integral backstepping sliding mode algorithm," *IEEE Access*, vol. 8, pp. 51352–51362, 2020.

[30] P. Leng, Y. Li, D. Zhou, J. Li, and S. Zhou, "Decoupling control of maglev train based on feedback linearization," *IEEE Access*, vol. 7, pp. 130352–130362, 2019.

[31] Y. Sun, Z. He, J. Xu, F. Li, and D. Zhang, "Cooperative model predictive levitation control for two-points electromagnetic levitation system of high-speed maglev vehicle," *IEEE Trans. Intell. Vehicles*, early access, Nov. 6, 2023, doi: 10.1109/TIV.2023.3329073.

[32] J. Ding, X. Yang, and Z. Long, "Structure and control design of levitation electromagnet for electromagnetic suspension medium-speed maglev train," *J. Vib. Control*, vol. 25, no. 6, pp. 1179–1193, Mar. 2019.

[33] C. Chen, J. Xu, L. Rong, W. Ji, G. Lin, and Y. Sun, "Neural-network-state-observation-based adaptive inversion control method of Maglev train," *IEEE Trans. Veh. Technol.*, vol. 71, no. 4, pp. 3660–3669, Apr. 2022.

[34] Y. Xu, Z. Zhao, Z. Long, and T. Wen, "Performance optimization of maglev train's electromagnetic levitation system: Control structure and algorithm," *IEEE Trans. Autom. Sci. Eng.*, vol. 21, no. 3, pp. 2507–2517, Apr. 2023.

[35] H.-W. Li, A. Maghareh, H. Montoya, J. W. C. Uribe, S. J. Dyke, and Z.-D. Xu, "Sliding mode control design for the benchmark problem in real-time hybrid simulation," *Mech. Syst. Signal Process.*, vol. 151, Apr. 2021, Art. no. 107364.

[36] M. Crescentini, S. F. Syeda, and G. P. Gibiino, "Hall-effect current sensors: Principles of operation and implementation techniques," *IEEE Sensors J.*, vol. 22, no. 11, pp. 10137–10151, Jun. 2022.

[37] H.-W. Li, A. Maghareh, J. W. C. Uribe, H. Montoya, S. J. Dyke, and Z.-D. Xu, "Advancing real-time hybrid simulation for coupled nonlinear soil-isolator-structure system," *Smart Struct. Syst.*, vol. 28, no. 1, pp. 105–119, Jul. 2021.

[38] H.-W. Li, A. Maghareh, J. W. C. Uribe, H. Montoya, S. J. Dyke, and Z.-D. Xu, "An adaptive sliding mode control system and its application to real-time hybrid simulation," *Struct. Control Health Monitor.*, vol. 29, no. 1, p. 2851, Jan. 2022.

[39] F. Zhao, K. You, S. Song, W. Zhang, and L. Tong, "Suspension regulation of medium-low-speed maglev trains via deep reinforcement learning," *IEEE Trans. Artif. Intell.*, vol. 2, no. 4, pp. 341–351, Aug. 2021.

[40] A. D'Alessandro et al., "Characterization of MEMS accelerometer self-noise by means of PSD and Allan variance analysis," in *Proc. 7th IEEE Int. Workshop Adv. Sensors Interfaces (IWASI)*, Jun. 2017, pp. 159–164.

[41] S. Albatran, A. Alatoum, and A. R. A. Khalaileh, "Informative order-reduction of underdamped third-order systems," *IEEE Access*, vol. 9, pp. 88512–88523, 2021.

Hong-Wei Li received the B.S. and Ph.D. degrees in civil engineering from Southeast University, Nanjing, China, in 2014 and 2021, respectively. He is currently a Research Assistant Professor with The Hong Kong Polytechnic University, Hong Kong, China. His research interests include structural health monitoring, structural dynamics, and nonlinear control.

Duo Zhang received the B.S. degree in traffic and transportation and the Ph.D. degree in traffic and transportation planning and management from Southwest Jiaotong University, Chengdu, China, in 2012 and 2020, respectively. He is currently a Post-Doctoral Fellow with the National Engineering Research Center on Rail Transit Electrification and Automation (Hong Kong Branch), The Hong Kong Polytechnic University, Hong Kong, China. His research interests include vehicle system dynamics, noise and vibration control, and monitoring and control in rail engineering.

Yang Lu received the B.S. degree in civil engineering from Shenyang Jianzhu University, Shenyang, China, in 2014, and the M.Sc. degree in civil engineering from The Hong Kong Polytechnic University, Hong Kong, China, in 2018, where he is currently pursuing the Ph.D. degree in civil and environmental engineering. His research interests include maglev levitation control, dynamics of maglev systems, and structural health monitoring.

Yi-Qing Ni (Member, IEEE) received the B.Eng. degree in structural engineering and the M.S. degree in structural dynamics from Zhejiang University, Hangzhou, China, in 1983 and 1986, respectively, and the Ph.D. degree in structural dynamics from The Hong Kong Polytechnic University, Hong Kong, China, in 1997. He is currently a Yim, Mak, Kwok, and Chung Professor of smart structures with The Hong Kong Polytechnic University. He is the Director of the National Engineering Research Center on Rail Transit Electrification and Automation (Hong Kong Branch), Hong Kong, and the Vice President of the International Society for Structural Health Monitoring of Intelligent Infrastructure. His research interests include structural health monitoring, structural dynamics and control, smart materials and structures, sensors and actuators, and monitoring and control in railway engineering.

Zhao-Dong Xu received the B.S. and Ph.D. degrees in civil engineering from Xi'an University of Architecture and Technology, Xi'an, Shaanxi, China, in 1996 and 2000, respectively. He is currently a Professor with Southeast University, Nanjing, China. He is the Director of China–Pakistan Belt and Road Joint Laboratory on Smart Disaster Prevention of Major Infrastructures, Nanjing. His research interests include structural health monitoring, structural dynamics and control, and smart disaster prevention.

Qi Zhu received the B.S. degree in civil engineering and the M.S. degree in bridge and tunnel engineering from Zhejiang University, China, in 2018 and 2021, respectively. She is currently pursuing the Ph.D. degree in civil and environmental engineering with The Hong Kong Polytechnic University, Hong Kong, China. Her research interests include maglev trains, deep reinforcement learning, and multi-agent cooperative control.

Su-Mei Wang (Member, IEEE) received the B.S. degree in civil engineering from Hebei University, Baoding, China, in 2013, and the Ph.D. degree in bridge and tunnel engineering from Zhejiang University, Hangzhou, China, in 2018. She is currently a Research Assistant Professor with The Hong Kong Polytechnic University, Hong Kong, China. Her research interests include structural health monitoring, high-speed railway and maglev structural dynamics, the interaction of train-rail-bridge systems, vision-based deep learning, and monitoring and control in rail engineering.